WindSat Radio-Frequency Interference Signature and Its Identification Over Land and Ocean

L. Li, *Member, IEEE*, Peter W. Gaiser, *Senior Member, IEEE*, Michael H. Bettenhausen, *Member, IEEE*, and William Johnston

***Abstract*—Radio-frequency interference (RFI) in the spaceborne multichannel radiometer data of WindSat and the Advanced Microwave Scanning Radiometer–EOS is currently being detected using a spectral difference technique. Such a technique does not explicitly utilize multichannel correlations of radiometer data, which are key information in separating RFI from natural radiations. Furthermore, it is not optimal for radiometer data observed over ocean regions due to the inherent large natural variability of spectral difference over ocean. In this paper, we first analyzed multivariate WindSat and Scanning Multichannel Microwave Radiometer (SMMR) data in terms of channel correlation, information content, and principal components of WindSat and SMMR data. Then two methods based on channel correlation were developed for RFI detection over land and ocean. Over land, we extended the spectral difference technique using principal component analysis (PCA) of RFI indices, which integrates statistics of target emission/scattering characteristics (through RFI indices) and multivariate correlation of radiometer data into a single statistical framework of PCA. Over ocean, channel regression of X-band can account for nearly all of the natural variations in the WindSat data. Therefore, we use a channel regression-based model difference technique to directly predict RFI-free brightness temperature, and therefore RFI intensity. Although model difference technique is most desirable, it is more difficult to apply over land due to heterogeneity of land surfaces. Both methods improve our knowledge of RFI signatures in terms of channel correlations and explore potential RFI mitigation, and thus provide risk reductions for future satellite passive microwave missions such as the NPOESS Conical Scanning Microwave Imager/Sounder. The new RFI algorithms are effective in detecting RFI in the C- and X-band Windsat radiometer channels over land and ocean.**

***Index Terms*—Microwave remote sensing, radio-frequency interference (RFI), WindSat.**

I. Introduction

DURING the past several decades, many satellite microwave radiometers have been launched into space. The Scanning Multichannel Microwave Radiometer (SMMR) was launched in 1978 to collect data at four frequencies from 6.8–37 GHz [1]. A series of the Special Sensor Microwave/Imager (SSM/I) instruments have been collecting data from 19–85 GHz for more than 15 years [2]. In 2002, the National Space Development Agency of Japan launched the Advanced Microwave Scanning Radiometer–EOS (AMSR-E) onboard the National Aeronautics and Space Administration Earth Obsering System Aqua satellite [3]. In 2003, the U.S. Naval Research Laboratory (NRL) launched the WindSat radiometer on the Department of Defense Coriolis satellite [4]. Except for SSM/I, the other sensors have included C- and X-band channels to enhance surface sensing capabilities. WindSat is the first spaceborne polarimetric radiometer that measures the third and fourth components of the modified Stokes vector in addition to the first two components of vertical and horizontal brightness temperature. It can be viewed as a successor in technology to SSM/I and AMSR-E with extended polarimetric capabilities for detecting ocean surface wind directions. WindSat is also a risk reduction mission to the next-generation polarimetric radiometer mission, the Conical Scanning Microwave Imager/Sounder (CMIS) [5], [6], planned for launch as part of the National Polar-orbiting Operational Environmental Satellite System (NPOESS) in the 2009 time frame. Table I provides a comparison of sensor characteristics. In the table $T_{\rm V}, T_{\rm H}$, U, and F denote vertical, horizontal, third, and fourth Stokes parameters, respectively. Except for their difference in polarimetric capabilities, AMSR-E, WindSat, and CMIS are all functionally quite similar in terms of frequencies, viewing configurations, and spatial resolutions.

TABLE I
SPACEBORNE PASSIVE MICROWAVE SENSOR CHARACTERISTICS

Frequency (GHz)	SMMR	SSM/I	AMSR-E	WindSat
	Channels			
85/91	-	TB_V, TB_H	TB_V, TB_H	-
37	TB_V, TB_H	TB_V, TB_H	TB_V, TB_H	TB_V, TB_H, U, F
22/23	TB_V, TB_H	TB_V, TB_H	TB_V, TB_H	TB_V, TB_H
19	TB_V, TB_H	TB_V, TB_H	TB_V, TB_H	TB_V, TB_H, U, F
10.8	TB_V, TB_H	-	TB_V, TB_H	TB_V, TB_H, U, F
6.8	TB_V, TB_H	-	TB_V, TB_H	TB_V, TB_H
37 IFOV, km	27x18	27x38	8x14	8x13
Absolute Accuracy	2.0 K	1.5 K	1.0 K	0.75 K

In recent years, due to the increasing conflict between scientific and commercial users of the radio spectrum, radio-frequency interference (RFI) has become a serious problem for microwave radiometry. Postlaunch AMSR-E data analysis revealed for the first time very strong and widespread RFI in the C- and X-band observations, which were also seen in WindSat measurements. If not properly identified and rejected, this RFI contamination problem could significantly reduce the science value of existing and future C- and X-band passive microwave missions. To this end, a spectral difference technique has been developed for AMSR-E to quantify the RFI magnitude and extent over the U.S. and global land areas [7], [8]. A similar

Manuscript received February 7, 2005; revised October 20, 2005. This work was supported in part by the National Polar-orbiting Operational Environmental Satellite System Integrated Program Office and in part by the Naval Research Laboratory Ocean and Atmospheric Science and Technology Program.

L. Li, P. W. Gaiser, and M. H. Bettenhausen are with the Naval Research Laboratory Washington, DC 20375 USA (e-mail: li.li@nrl.navy.mil).

W. Johnston is with Computational Physics, Inc., Springfield, VA 22151 USA.

Digital Object Identifier 10.1109/TGRS.2005.862503

method was also used to survey WindSat land RFI over the U.S. [9]. Despite its effectiveness in detecting these types of RFI, such a spectral difference technique was applied only to detect land RFI; it is not optimal for ocean RFI due to inherent large natural variability of the spectral difference over the ocean.

The principle of spectral difference RFI detection technique is based on the distinct signature differences between natural radiation and RFI induced by human activities. Because the RFI has narrower bandwidth relative to natural radiation, its emission/scattering characteristics are very different, resulting in negative spectral gradient [7], [10]. Equally important, natural radiation can be characterized by high correlations among different radiometer channels; while RFI tends to be decorrelated with natural variations. By examining variations of channel correlation and spectral gradient, the spectral difference technique defines the negative spectral gradient as an RFI index (RI), and RFI is detected if the RI exceeds a threshold beyond its natural variation [7]. The threshold determination does not use information from the correlation between channels.

The principal components analysis (PCA) is an efficient tool for analyzing the channel correlation of the multivariate radiometer data. It decomposes multichannel data into a number of orthonormal components according to their correlations, and separates RFI components from natural variations more efficiently and consistently. By incorporating PCA in the spectral difference technique, we can integrate statistics of target emission/scattering characteristics (through RFI indices) and multivariate correlation of radiometer data into a single statistical framework. This methodology will be used in C-band RFI detection over land. Over ocean, the channel correlations are sufficiently high and can be used to predict RFI-free measurements with small uncertainty.

The model difference technique defines the difference between measured and predicted brightness temperatures as RFI Intensity [11]. It has the advantage of producing a more direct measure of the RFI intensity than the spectral difference or PCA techniques. However, the heterogeneity of land scenes causes model difference technique to have a higher prediction uncertainty than for ocean scenes. Therefore, despite being a preferred technique, model difference was only implemented to ocean scenes.

The vertical and horizontal polarization brightness temperatures respond directly to the RFI intensity, but the third and fourth Stokes parameters also respond to the polarization states of the RFI signals. The use of WindSat polarimetric channels to detect RFI is discussed in detail in [9]. In this paper we exclude polarimetric channels in our RFI detection algorithm. Section II discusses briefly the WindSat instrument and its data processing. Section III examines WindSat multivariate signatures in terms of channel correlations and principal component analysis, based on which land and ocean RFI detection algorithms are developed in Section IV. Finally, WindSat RFI results and their implications to CMIS risk reduction are discussed in Section V.

II. WindSat Instrument and Measurements

The WindSat instrument is the first and only spaceborne polarimetric microwave radiometer currently in operation [4]. It is designed to demonstrate the capability of polarimetric microwave radiometry in ocean vector wind sensing and should also have very significant value for land sensing. In addition to the SSM/I and AMSR-E dual-polarization microwave imager frequency bands, WindSat provides fully polarimetric measurements at 10.7, 18.7, and 37.0 GHz, and additional dual-polarization measurements at 6.8 and 23.8 GHz. Each channel is first individually calibrated, geolocated, and quality controlled to produce antenna temperatures at its footprint resolution. Then, all the channels are further processed for antenna pattern correction, data resampling, and beam averaging to generate brightness temperature data at a common spatial resolution, called Sensor Data Record (SDR) [4]. In this study, we used SDR version 1.6.1 data coregistered to a common spatial resolution of 40 km $\times$ 60 km. Following the SDR processing, we binned the swath data onto the global 25-km EASE grid and composed them into separate daily ascending and descending data files.

For comparison with WindSat data, we acquired the historical SMMR multichannel brightness temperature data from the National Snow and Ice Data Center. The data were processed using a similar binning method and the 25-km EASE grid format [12]. SMMR had vertical and horizontal polarization channels at five frequencies, 6.6, 10.7, 18, 21, and 37 GHz, which are very similar to WindSat frequencies. However, SMMR spatial resolutions are very different for each frequency. They are 148 km $\times$ 95 km, 91 km $\times$ 59 km, 55 km $\times$ 41 km, 46 km $\times$ 30 km, and 27 km $\times$ 18 km from 6.6–37 GHz, respectively. These footprints were not resampled to a common resolution as was WindSat. Nevertheless, the SMMR data were much less contaminated by RFI during its mission from 1978 to 1987. Therefore, it is interesting to compare the statistics of Windsat measurements against those of SMMR.

III. Multivariate Signatures of RFI and Natural Radiation

A. RFI and Natural Radiation Characteristics

Man-made radiation from active microwave transmitters (or RFI to a radiometer) is distinctly different from natural radiation in terms of intensity, spatial variability, spectral characteristics, and channel correlations. RFI signals typically originate from a wide variety of coherent point target sources, i.e., radiating devices and antennas, and are often directional, isolated, narrowband, and coherent. On the other hand, as distributed targets, the Earth's surfaces often produce smooth, ultrawideband, and incoherent microwave radiation. At 30 GHz and below, scattering effects from natural targets are relatively weaker than the emission signals. RFI can increase brightness temperatures significantly at a particular frequency and generate negative spectral gradient [7], which can be used to identify RFI when such scattering signatures, in terms of the spectral differences, and its spatial variations (standard deviation), are beyond their natural variability [7], [8]. This method is called the spectral difference technique. For example, land RFI is identified for the 6-GHz AMSR-E vertical polarization channel if the mean and standard deviation of RFI Index, $\mathrm{RI}_{06V} = TB_{06V} - TB_{10V}$, exceed 3-K threshold [8]. The exact threshold used depends on the radiometer sensitivity and channels, the application, and the

TABLE II
(a) SMMR CHANNEL CORRELATION MATRIX. (b) WINDSAT CHANNEL CORRELATION MATRIX. (c) WINDSAT CHANNEL CORRELATION MATRIX FOR RFI-CONTAMINATED DATA

	06V	10V	18V	23V	37V
06V	1.0000	0.90663	0.87311	0.87466	0.82429
10V		1.00000	0.98356	0.97336	0.94047
18V			1.00000	0.98527	0.96687
23V				1.00000	0.96350
37V					1.00000
	06H	10H	18H	23H	37H
06H	1.00000	0.88686	0.81566	0.78880	0.73478
10H		1.00000	0.97116	0.94120	0.90328
18H			1.00000	0.97811	0.96023
23H				1.00000	0.96246
37H					1.00000

(a)

	06V	10V	18V	23V	37V
06V	1.00000	0.77312	0.72860	0.71902	0.67152
10V		1.00000	0.96676	0.93918	0.91008
18V			1.00000	0.97252	0.96492
23V				1.00000	0.96721
37V					1.00000
	06H	10H	18H	23H	37H
06H	1.00000	0.74996	0.68930	0.618507	0.62052
10H		1.00000	0.93954	0.869684	0.89056
18H			1.00000	0.940392	0.95611
23H				1.00000	0.95581
37H					1.00000

(b)

	06V	10V	18V	23V	37V
06V	1.0000	0.39787	0.29046	0.29746	0.27322
10V		1.00000	0.94306	0.90370	0.90657
18V			1.00000	0.95555	0.97806
23V				1.00000	0.95197
37V					1.00000
	06H	10H	18H	23H	37H
06H	1.00000	0.39219	0.23143	0.13380	0.22794
10H		1.00000	0.86850	0.73357	0.85463
18H			1.00000	0.91799	0.96443
23H				1.00000	0.92042
37H					1.00000

(c)

natural scene. From multivariate perspective, the natural microwave radiation measured by each radiometer channel is governed by the naturally occurring geophysical processes, and thus has very well defined interchannel correlations. An RFI signal, due to its relatively narrow bandwidth, tends to be independent and decorrelated with the natural variations.

Since the SMMR mission ended in 1987 prior to today's proliferation of microwave sources and no RFI contamination was found in SMMR data over the U.S., we compared SMMR channel correlation against those of WindSat. Only SMMR and WindSat data over the U.S. were used in such a comparison. Ten-day composite EASE-Grid data were generated for SMMR and WindSat using EASE-Grid data from July 1–10, 1979 and 2003, respectively. We used ten days of SMMR data to have a complete global coverage because the SMMR instrument was switched on and off on alternate days due to power sharing constraints among different instruments on the spacecraft. Ocean and coastal pixels were removed from this data to focus on the multicorrelations of land data. Table II compares SMMR and WindSat correlation matrices for vertical and horizontal channels. In Table II(a), for SMMR, all the channels are positively and highly correlated, and correlations are higher for vertical polarization than horizontal. For C-band vertical brightness temperatures, the correlation decreases from 0.91 to 0.82 as the frequency increases. For C-band horizontal brightness temperature, the correlation varies from 0.88 to 0.73. Higher frequency SMMR channel correlation is mostly above 0.95. In the case of WindSat in Table II(b), similar high correlations remain evident except for the RFI-contaminated C-band channels, which have significantly decreased correlations against all other channels. To further examine the channel correlations in RFI-contaminated regions, we recalculated the WindSat correlation matrix using only RFI-contaminated data points where the RFI Index $T_{B06} - T_{B10}$ exceeds 10 K for both vertical and horizontal polarizations. The result is shown in Table II(c). Clearly, the two C-band channels have virtually no correlation with higher frequency channels. The highest correlation is only 0.398 between C- and X-band vertical polarizations channels; other C-band channel correlations vary between 0.13 and 0.29. Except for the C-band channels, correlations between other channels remain quite high around 0.9. Therefore, the RFI signal is indeed decorrelated with natural radiation in the contaminated areas, showing channel correlation as critical information in distinguishing RFI from natural radiation.

TABLE III
WINDSAT CHANNEL CORRELATION MATRIX FOR RFI-FREE OCEAN DATA

	06V	10V	18V	23V	37V
06V	1.0000	0.99090	0.96036	0.92926	0.92540
10V		1.00000	0.97958	0.95234	0.94850
18V			1.00000	0.99293	0.98894
23V				1.00000	0.99539
37V					1.00000
	06H	10H	18H	23H	37H
06H	1.00000	0.99084	0.96445	0.92000	0.93513
10H		1.00000	0.98444	0.94918	0.96189
18H			1.00000	0.98733	0.99105
23H				1.00000	0.99393
37H					1.00000

Table III shows the WindSat channel correlation matrix for global RFI-free ocean measurements from June 20–29, 2004. In general, the correlations are extremely high, mostly between 0.95 and 0.99. For convenience, let us denote 6.8- and 10.7-GHz channels as surface channels and 18 GHz and above as atmospheric channels. We can see that channel correlations within the surface or atmospheric channels separately are in the 0.97 to 0.99 range. The correlations between surface and atmospheric channels are less, but still above 0.93. These extremely high channel correlations will provide us an excellent opportunity to implement the channel regression based model difference method, shown in Section IV.

B. Principal Component Analysis

PCA is a statistical technique that linearly transforms a set of correlated variables into a smaller set of uncorrelated variables that forms a new orthonormal data space. In this new data space, the first basis vector spans in the direction of maximum variance in the data. Each successive basis vector spans the direction of largest variance not accounted for by the previous vectors. This new set of variables, or basis vectors, are called principal components [13], which can be constructed using eigenvalue/eigenvector decomposition. The size of each eigenvalue determines

the variance of the corresponding principal component. If we assume that information in data is represented by its variance, eigenvalues can be used to quantify informational content for each principal component. PCA is commonly used to reduce data dimensionality, computational complexity and the noise levels. It can also be used in cluster identification and classifications. In our case of RFI detection, we seek to extract the RFI-related principal component in multidimensional radiometer data. But first let us examine the multichannel WindSat brightness temperatures in terms of its principal components, and its variance or information content.

For a given set of multichannel radiometer data, the original data vector is given by

$$\bar{T} = [T_{B1}, T_{B2}, \ldots, T_{Bn}]^t \tag{1}$$

where $T_{Bi}, i = 1, \ldots, n$, represents the brightness temperatures of different frequency and polarization channels, n is the number of the data channel to be analyzed, and t denotes the transpose operation. In our case, a ten-channel SMMR or WindSat data vector is defined as $\bar{T} = [TB_{06V}, TB_{06H}, TB_{10V}, TB_{10H}, TB_{18V}, TB_{18H}, TB_{23V}, TB_{23H}, TB_{37V}, TB_{37H}]$. Letting the covariance matrix be denoted as $\Sigma_{\vec{T}}$, the eigenvalue and eigenvector are found in equation

$$\Sigma_{\vec{T}} A = A\Lambda \tag{2}$$

where A is the eigenvector matrix and Λ the diagonal eigenvalue matrix. Once the eigenvalues and eigenvectors are obtained, the original data vector $\vec{T}$ can be projected onto the new basis vectors in principal component space

$$S = A^t \bar{T}. \tag{3}$$

The elements of S are often referred as the principal component scores. For RFI-related principal components, the score is high when RFI is present and low when it is not.

Since channel correlations are key information in detecting RFI, it is interesting to examine them in terms of information content using PCA. It is also interesting to compare RFI-contaminated Windsat data with RFI-free SMMR data. However, one must remember that different SMMR channels are not resampled to the same footprint resolution as WindSat, and thus have different spatial resolutions for different frequency. In other words, the different SMMR channels do not observe a given target at the same time and location. Such a difference in resolution will introduce distortions to SMMR channel correlations, which are especially pronounced when the satellite passes over a strong storm system or land/water boundary. Therefore, the differences between WindSat and SMMR can not be attributed entirely to RFI influence. Nevertheless, these two satellites have very similar vertical and horizontal polarized channels at the five similar frequencies as shown in Table I. Without RFI corruption, their natural radiation signature should be similar, which is illustrated here with the WindSat and SMMR signatures over land. To better contrast the signatures of RFI and natural radiation, only EASE-Grid WindSat and SMMR data over the U.S. were used in the PCA for this specific comparison. Ocean and coastal region data are also masked out in this data analysis.

Fig. 1(a) illustrates resulting eigenvalue spectrum for WindSat (the solid line) and SMMR (the dotted line). Fig. 1(b) shows the

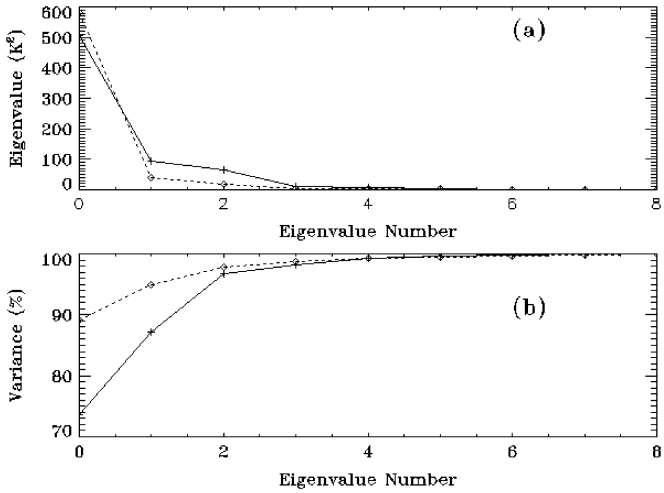

Fig. 1. Comparisons of WindSat and SMMR eigenvalues and variance. WindSat data are indicated by a solid line and SMMR by a dotted line.

percent of total variance accounted for by each principal component. The eigenvalues are similar and drop very quickly for both sensors: therefore, a majority of data variance is contained the first few principal components. Eigenvalues that are less than 4 K^2 for SMMR and 0.4 K^2 for WindSat are below the specified instrument noise level. Out of ten-channel radiometer data, the top three components account for more than 96% of the variance for both sensors, confirming the high channel correlations. Nevertheless, the SMMR eigenvalues drop faster than WindSat, which indicates less variance or information in SMMR data than in WindSat. This is consistent with the fact that there is no RFI information in the selected SMMR dataset.

Fig. 2 plots the coefficients of top three SMMR (dotted line) and WindSat (solid line) principal components. Their corresponding variances were plotted in Fig. 1(a). Higher order components account for only 2.2% of the total variance for SMMR and 3.3% for WindSat. Therefore they are not plotted here. In general, each component responds to the combination of three variables with different emphasis: the overall magnitude of all radiometer channels, the spectral gradient, and the polarization difference. When a component responds to overall magnitude, its coefficients are all positive. The horizontal polarization channels can have larger coefficients than vertical since their data variances are usually larger. Responding to the spectral gradient means the coefficients decrease with frequency. If the coefficients have opposite sign for vertical and horizontal channels, the component is responding to the polarization difference.

Clearly, there is a significant difference in first principal component between SMMR and Windsat, but their second and third principal components are very similar. Similar SMMR principal component signatures were also found over sea ice regions in the Arctic [14]. The first SMMR and WindSat components emphasize the overall magnitude. All the coefficients are positive and of similar magnitude for vertical (odd-numbered channels) and horizontal (even-numbered channels) polarizations. SMMR coefficients are quite flat for all channels, but WindSat coefficients decrease with frequency and are higher for vertical polarization than horizontal. The 6.8-GHz channels are weighted much more than the rest of the channels, showing that WindSat first principal

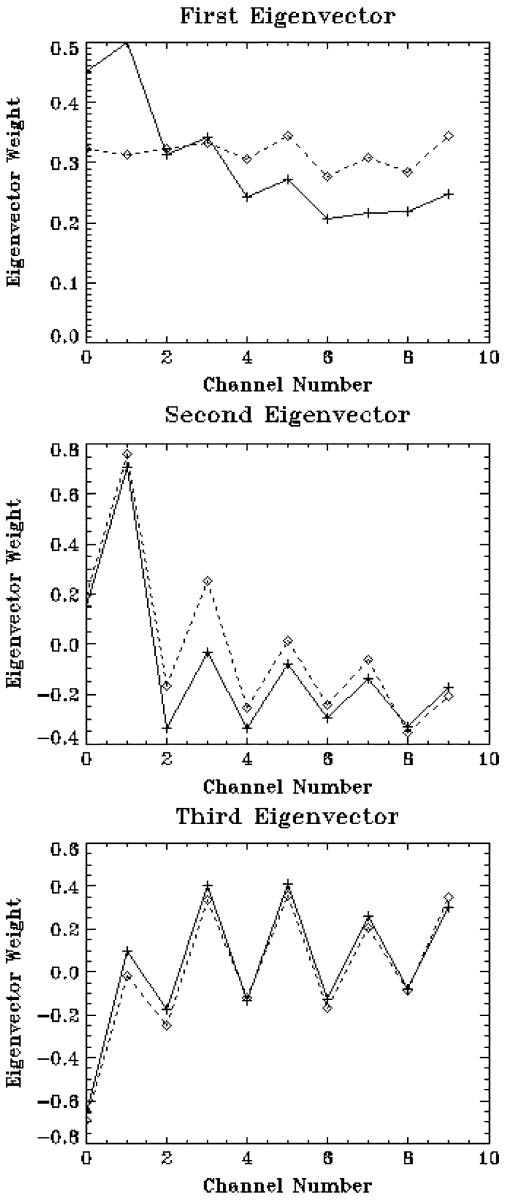

Fig. 2. Comparisons of WindSat and SMMR eigenvectors. WindSat data are indicated by a solid line and SMMR by a dotted line.

component contains some spectral gradient and polarization information. From Fig. 1, the SMMR first component has 24.14-K standard deviation, accounting for 89% of the variance. For WindSat first component, the standard deviation is about 22.47 K accounting for 73% of the variance. The SMMR and Windsat second principal components respond strongly to the spectral gradient. For 10-GHz and higher channels, the negative coefficients emphasize vertical over horizontal polarizations. Since vertical polarization is much less sensitive to environmental variations than horizontal, such a coefficient structure will act to reduce the natural radiation background against the RFI signals. The standard deviations of the second components are 6.2 K (6% of total variance) and 9.7 K (14% of total variance) for SMMR and WindSat, respectively. The third eigenvector has negative coefficients for vertical polarization channels and positive for horizontal ones, therefore it highlights the difference between the polarizations and acts as a measure of the polarization signal.

IV. RFI Identification Over Land and Ocean

A. Spectral Difference Technique

Spectral difference and channel correlation are two pieces of key information for RFI identification. Previous land RFI identification algorithms were based mostly on the spectral differences or RFI indices [7]–[9]. Channel correlation was not used to establish the threshold values for the RFI Indices. For such a spectral difference technique to be effective in identifying RFI, the natural variability of spectral differences has to be relatively small compared to RFI signatures, which is indeed the case for land multivariate radiometer data. However, over the ocean, spectral differences can change significantly with ocean surface conditions (wind speed and direction) and atmospheric events (water vapor, cloud, and precipitation), creating high natural variation or large inherent uncertainties in RFI indices. Therefore, the spectral difference technique has not been previously used in ocean RFI identification.

To understand the natural variability of the RFI-free spectral differences, we calculated the normalized histogram of SMMR and WindSat RFI index $\mathrm{RI}_{10H} = TB_{10H} - TB_{18H}$ from the ten-day composite global EASE-Grid data that we have used in previous section. In this case, global brightness temperatures are separated into two groups of land and ocean data using a static 10-km land mask dataset. Sea ice, land ice, island, and coastal regions were excluded from the data. It is to be noted that most of the 10-GHz RFI in the WindSat data in and around Europe were removed from the data by a $\pm$270-km coastal mask. Therefore, the RFI distortion of the statistics should be limited. Fig. 3(a) plots the normalized histogram of SMMR and WindSat RFI index RI_{10H}. The solid and dashed lines are for WindSat and SMMR spectral differences, respectively. The land spectral difference statistics for both sensors are close to a Gaussian distribution and have standard deviations of 3.2 K for SMMR and 4.7 K for WindSat. For the ocean spectral difference, its statistics do not follow the Gaussian distribution and have standard deviations of 9.4 K for SMMR and 14.5 K for WindSat, which are about three times larger than their land spectral differences for both sensors, highlighting the large natural variability of the ocean spectral difference relative to land. Unlike land data histograms, there are apparent disagreements on ocean histograms between SMMR and WindSat, which are reflections of different beamfilling effects for the two sensors. Over ocean, light to moderate rain (less than 8 mm/h) can generate RFI index RI_{10H} as high as 90 K, while RI_{10H} over land is mostly less than 15 to 20 K. Therefore, beamfilling affects RI_{10H} histograms much more over ocean than land.

Since Siberia has always been relatively RFI-free, we also compared SMMR and WindSat spectral differences in this region, which is defined by latitude between 62° N and 72° N and longitude between 90° E and 125° E. The data were extracted from seven data-days covering July 1–7, 2003 for WindSat and July 1–14, 1979 for SMMR (note that SMMR instrument was switched on-and-off on alternate days). The 10-km land mask dataset was again used to remove nonland pixels. Fig. 3(b) compares the normalized histogram of RFI index RI_{10H} for WindSat (solid line) and SMMR (dashed line) over the Siberia region, which shows very consistent statistics of spectral differences for

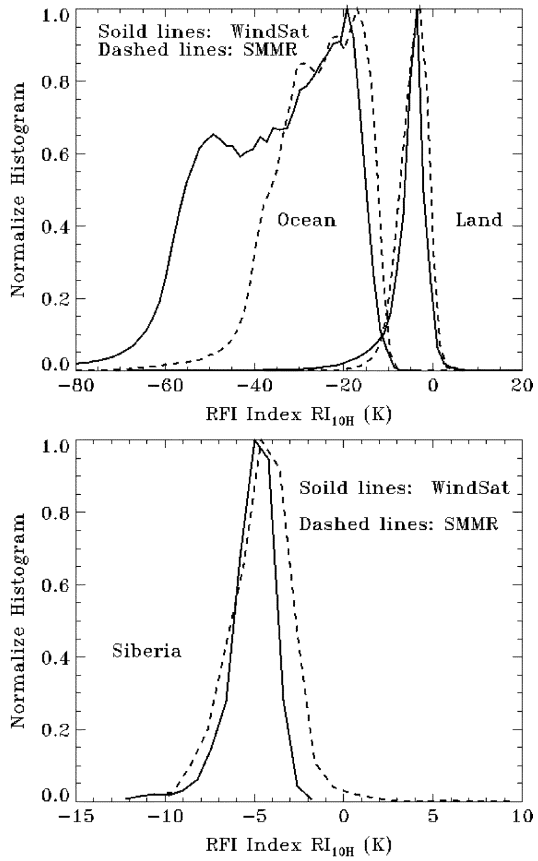

Fig. 3. Normalized histogram of RFI index. (a) (Solid line) WindSat and (dashed line) SMMR RI_{10H} over global land and ocean. (b) RI_{10H} over Siberia, Russia for (solid line) WindSat and (dashed line) SMMR.

both sensors. The standard deviations are 1.4 K for WindSat and 1.8 K for SMMR. Their mean are also very consistent, being -5.2 and -4.6 K, respectively. Therefore, WindSat and SMMR have very consistent statistics on RFI-free spectral difference.

B. PCA-Based Land RFI Detection

In principle, RFI identification relies on two kinds of information. The first one is the emission/scattering characteristics represented by RFI indices, which is the physical information determined by the Earth materials and structures of the natural targets. The second one is the correlations between different channels or indices, which is the statistical information introduced by natural variability of the targets. The spectral difference technique contrasts RFI and natural radiation through emission/scattering signature and thus does not consider the statistical information. On the other hand, a statistics-based algorithm would consider only natural variability through independent principal components without using any physical information. Principal component analysis of RFI indices offers an elegant way to combine the spectral difference technique with channel correlation information. It generates an RFI-related principal component that is orthogonal to multivariate natural radiations, therefore integrating statistics of target emission/scattering characteristics and multivariate correlation of radiometer data into a single statistical framework.

The RFI indices used in the principal component analysis are $\mathrm{RI}_{6V} = TB_{6V} - TB_{10V}, \mathrm{RI}_{6H} = TB_{6H} - TB_{10H}, \mathrm{RI}_{10V} = TB_{10V} - TB_{18V}, \mathrm{RI}_{10H} = TB_{10H} - TB_{18H}, \mathrm{RI}_{18V} = TB_{18V} - TB_{23V}, \mathrm{RI}_{18H} = TB_{18H} - TB_{23H}, \mathrm{RI}_{23V} = TB_{23V} - TB_{37V}, \mathrm{RI}_{23H} = TB_{23H} - TB_{37H}$. Our goal is to define and separate two endmembers: RFI and RFI-free observations, which can be achieved through unsupervised analysis using all the pertinent WindSat data in and around the RFI-contaminated regions. To avoid coupling of RFI signals between vertical and horizontal polarizations, RI_{6V} and RI_{6H} were grouped into separated datasets with the rest of the RFI indices and used in two independent PCA studies, which have very similar results. RFI sources usually use polarized antennas. One wants to avoid coupling V and H channels so that one can better isolate the characteristics of the RFI. Furthermore, by performing the RFI detection separately for each polarization, one may find that only one of the two principal polarizations is contaminated. Therefore, only the case for horizontal polarization will be presented here. The input data vector is given by $\overline{V} = [\mathrm{RI}_{06H}, \mathrm{RI}_{10V}, \mathrm{RI}_{10H}, \mathrm{RI}_{18V}, \mathrm{RI}_{18H}, \mathrm{RI}_{23V}, \mathrm{RI}_{23H}, \mathrm{RI}_{37V}, \mathrm{RI}_{37H}]$, which represents a data cloud in a nine-dimensional space $\{V\}$. After the principal component decomposition, the data points in $\{V\}$ space can be projected to a new set of orthogonal coordinate, namely the principal component score (PCS)

$$\mathrm{PCS} = a_0 + \sum_i a_i \mathrm{RI}_{\mathrm{iv}} + \sum_i \mathrm{RI}_{\mathrm{ih}} \tag{4}$$

where i represents frequency from 6–37 GHz.

Fig. 4 shows the top three principal components of RFI indices of WindSat data over the U.S. The first principal component demonstrated a large contrast between large coefficients (near 1.0) of RFI-contaminated RI_{6H} and small coefficients (about 0.03 to 0.1) for rest of the RFI-free indices, which suggests that this component is PCA-identified RFI signal that is decorrelated with natural radiations. For the second and third principal components, the RI_{6H} coefficients are small or near zero, indicating RFI-free signatures. We also found that RI_{6H} coefficients of fourth or higher order components (not shown here) are all very small.

Once the multivariate RFI indices data are decomposed into orthogonal components, their information content and eigenvectors can be analyzed to identify the RFI-related principal components in a similar way to the process discussed in Section III. The principal component scores of the RFI components are then used to identify RFI-contaminated observations. Two RFI algorithms were developed from these PCA studies: C- and X-band land RFI algorithms. Each algorithm has separate sets of parameters for vertical and horizontal polarization.

WindSat PCA data analysis reveals widespread C-band land RFI in many regions of the world, particularly in the U.S., the Middle East, and Japan. As an example, Fig. 5(a) depicts C-band land RFI principal component score (RPCS) over the U.S. for horizontal polarization. RFI is identified for RPCS value greater than zero. Higher RPCS values indicate stronger RFI. These WindSat RFI distributions have many similarities to the ones found in AMSR-E data [7], which is reasonable since WindSat and AMSR-E have slightly different C-band center frequencies but significantly different bandwidth, which are 6.8 GHz with 125 MHz for WindSat and 6.9 GHz with 300 MHz for AMSR-E.

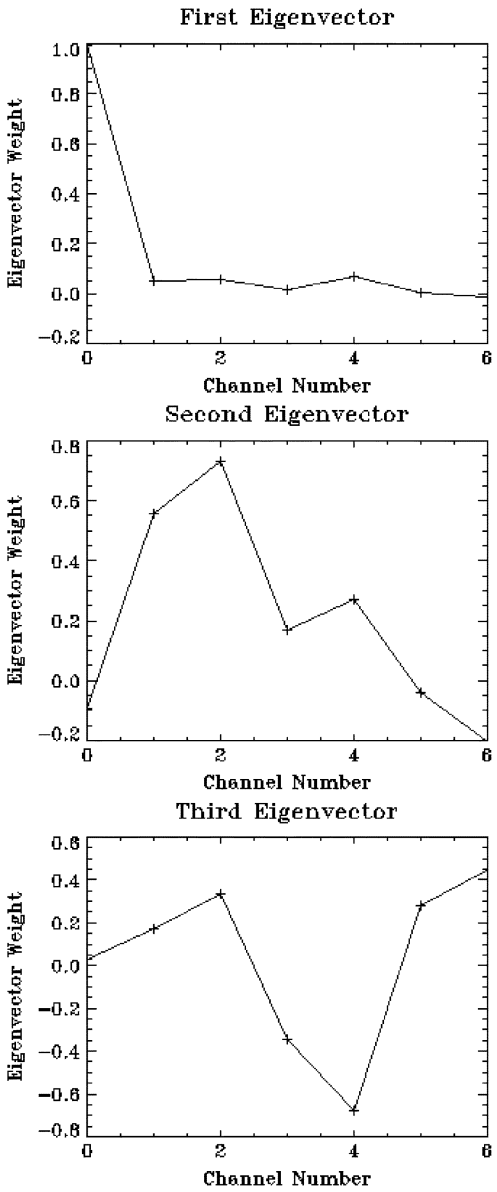

Fig. 4. Top three eigenvectors of WindSat RFI indices.

Most RFI are in or near cities or populated areas, and are persistent for every satellite overpass. Interestingly, while the U.S. shows a large amount of RFI, there is not much RFI in the neighboring countries of Canada and Mexico. Although there are no ground truth data available at this moment to objectively evaluate the existing RFI detection techniques, it is nevertheless informative to compare spectral difference and PCA-based methods in terms of their consistency and differences. Fig. 5(b) plots the absolute differences between PCA-based and spectral difference methods (PCA—Spectral Difference) for the RFI map shown in Fig. 5(a). Clearly, the difference changes with geophysical locations and is mostly under 2 K, although it can exceed 5 K at some locations. This small difference is consistent with the basic assumption of the spectral difference method, which is that the RFI index has small natural variability over land and can be used effectively to detect RFI except when it is weak. In other words, the difference of the two RFI techniques should be in the weak RFI range, as demonstrated in Fig. 5(b).

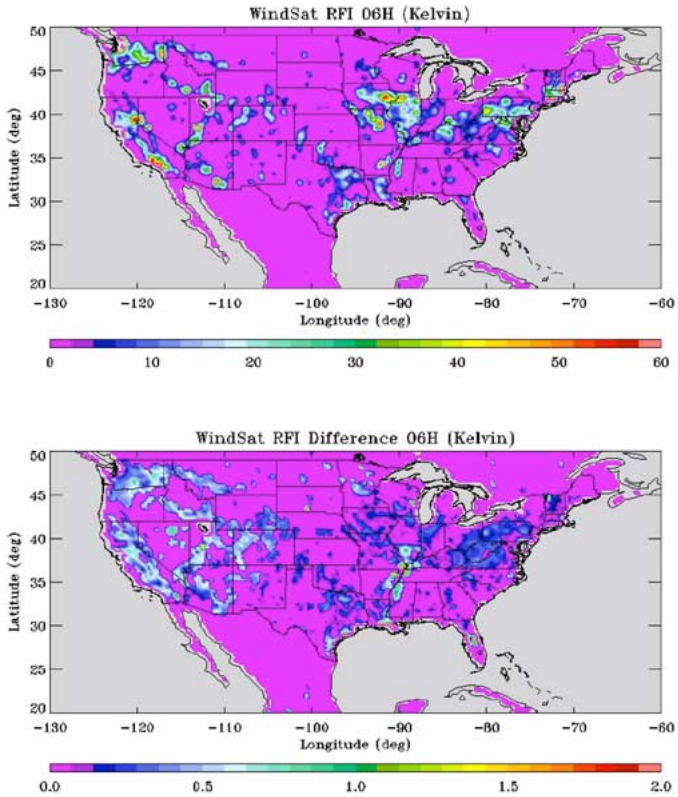

Fig. 5. WindSat C-band RFI distribution for horizontal polarization over the U.S. using (top panel) a PCA-based method and (bottom panel) the absolute difference between PCA-base and spectral difference methods (PCA minus Spectral Difference).

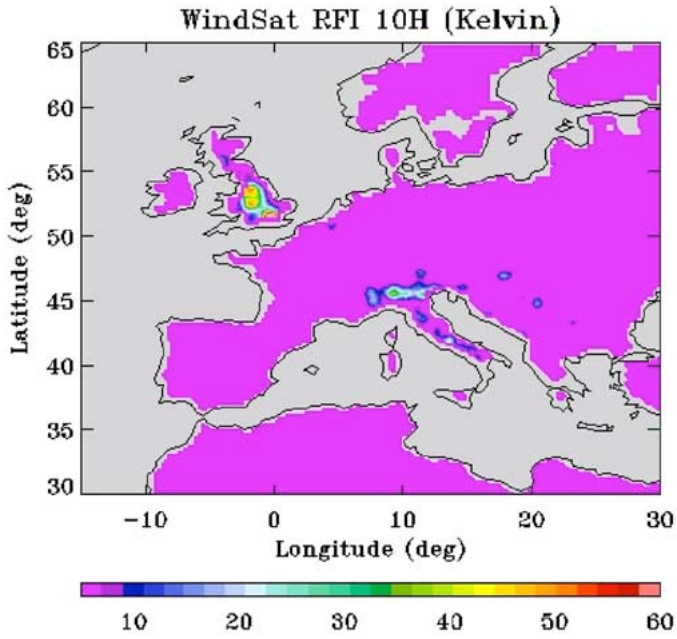

Fig. 6. WindSat X-band PCA-based RFI distribution for horizontal polarization over Europe.

WindSat X-band RFI is mostly found in Europe and Japan. Fig. 6 plots an X-band land RPCS map for horizontal polarization over Europe. In this case, RFI is defined where RPCS values are greater than 5. Similar to the C-band RFI, X-band RFI is again strongly correlated with geopolitical boundaries. There is

strong and widespread RFI in Great Britain and northern Italy. Some weaker RFI is found along Italy's coastal regions, and some spotty ones are seen in Bosnia. Overall, the RFI distribution over Europe is much sparser than the RFI seen over the U.S. It is also interesting that the RFI does not spread out into other parts of Europe, including northern England. However, such RFI maps often generate many intriguing questions about the source of these interference signals that are difficult to answer based on RFI distribution information alone. Exploring the linkage between observed RFI signals and man-made emitter sources is beyond the scope of this paper.

C. Model Difference Method for Ocean RFI Detection

The idea behind the model difference technique is to predict "RFI-free" brightness temperatures at a specific channel and define the positive difference between measured (TB) and predicted brightness temperature (FB) as RFI intensity RI $= (TB - \mathrm{FB})$ [11]. Because RFI intensity has physical interpretation, this technique is most desirable if the brightness temperature can be predicted with sufficient accuracy, which is indeed the case for ocean. Over the last decades, very well calibrated radiative transfer models have been developed that can "predict" brightness temperatures to within a few degrees. We can implement the model difference method using a radiative transfer model with inputs from results of numerical weather prediction or retrievals from other satellite sensors. Alternatively, we can utilize the very high channel correlations within the Windsat data, as demonstrated in Section III, and use RFI-free channels to predict the RFI corrupted data. This method does not need a radiative transfer model or ancillary dataset, and can be readily implemented using multichannel regressions [10], [11]. The second approach was used in this paper. We determined that oceans in the vicinities Europe and Argentina are RFI-contaminated regions since they are characterized by persistent high brightness temperature residuals in a radiative transfer-based ocean retrieval algorithm, which was developed for the WindSat [15]. Only rain-free conditions are considered by this algorithm. Excluding oceans near Europe and Argentina, the global oceans are assumed to be RFI-free. Six months of global RFI-free ocean data was collected from September 2003 to February 2004 excluding land, coastal region, and sea ice. These data were then used as a training dataset to regress X-band channels against the other WindSat channels. The predicted 10.7-GHz RFI-free brightness temperature is given by

$$TB_{10} = a_0 + \sum_i a_i TB_i + \sum_i b_i TB_i^2 + c_1 \ln(290 - TB_{23V}) + c_2 \ln(290 - TB_{23H}) \quad (5)$$

where TB_{10} is either the vertical or horizontal polarization brightness temperature. TB_i represents every WindSat channel except for those at 10.7- and 23.8-GHz frequencies. The regression errors have virtually zero mean and very small standard deviations, which are 0.48 and 0.75 K for the 10.7-GHz vertical and horizontal polarization channels, respectively. Such small errors indicate that the regression accounts for virtually all of the variance of the natural radiation. Next, this regression was applied to predict RFI-free brightness temperatures in the RFI-contaminated areas.

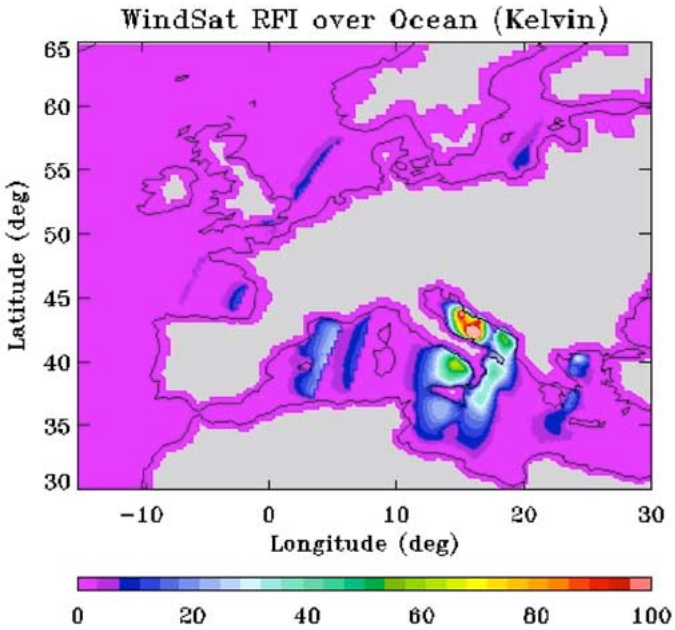

Fig. 7. WindSat X-band model difference-based RFI distribution for horizontal polarization over the Mediterranean Sea and North Sea.

We applied the model difference technique to WindSat ocean observations over Europe. Fig. 7 shows the RFI intensity map of WindSat X-band horizontal polarization data in descending passes from October 1–7, 2003. Clearly, there is very strong ocean RFI in the WindSat X-band data, mostly in the Mediterranean Sea. Three very bright RFI spots are located in the Adriatic Sea north of Italy, and some extensive ones around Sicily. The RFI locations and strength are also quite persistent for every satellite overpass with similar observation geometry, ruling out any mobile sources on the ocean. The likely sources of these RFI are broadcasting signals from European geostationary television (TV) satellites [16] above the equator. At microwave frequencies, the ocean surface has much larger reflectance than land surface due to the high permittivity value of seawater. Given the right viewing geometry and frequency, a spaceborne radiometer can observe strong satellite broadcasting signals reflected off the ocean surface, creating RFI over extended ocean areas. Such RFI was not found in the ascending pass of WindSat because the TV satellite signals are not in the forward looking direction of WindSat.

To illustrate that the spectral difference technique is ineffective in detecting ocean RFI, in Fig. 8 we calculated spectral difference or RFI Index $\mathrm{RI}_{10V} = TB_{10V} - TB_{06V}$ using the same data in Fig. 7 and compared it with the model difference technique in Fig. 7. As we can see, the spectral difference method can indeed detect much of the ocean RFI shown in Fig. 7, but it also misidentified a weather system at (9° W, 47° N) as RFI. There are also many misidentified RFI occurrences near coastal regions. At the global scale, we found similar misidentifications distributed all over the ocean with spatial patterns closely related to weather systems depicted by

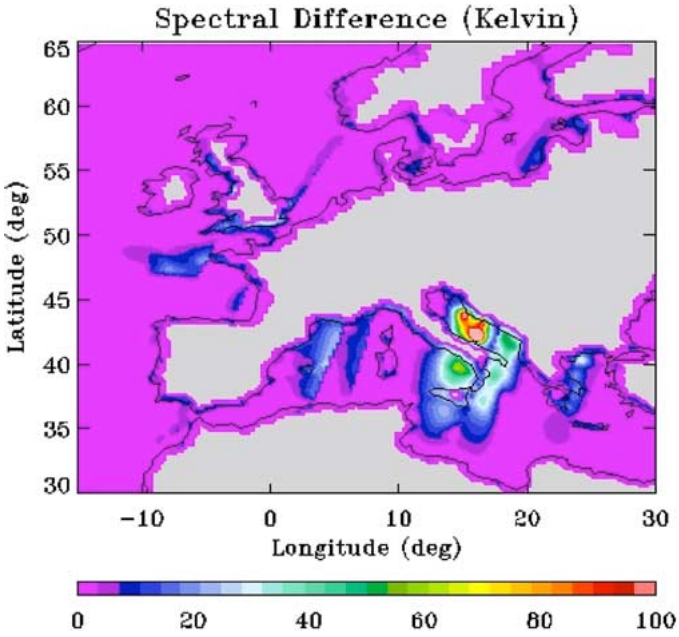

Fig. 8. Ocean RFI detections for X-band horizontal polarization using the spectral difference method.

ocean surface wind, cloud, and rain variations. We could certainly increase the RFI index threshold value to remove these "false alarm," but such an adjustment would also remove some moderate-level real RFI (below 15 K) in other regions. Therefore, spectral difference technique is not optimal for ocean RFI detection.

V. Conclusion

The RFI problem poses a significant challenge to current microwave missions including WindSat and AMSR-E, and will remain a serious issue for planned future microwave missions such as CMIS. A software/processing solution must be derived to identify and remove RFI since an RFI hardware solution is not likely to be able to suppress RFI globally and completely or even reduce it to an insignificant level, owing to either the availability or the cost of "perfect" RFI suppression technology [6]. To better identify WindSat RFI contamination, as well as provide risk reduction for CMIS, we need to fully understand and quantify the multivariate signatures of natural radiation and RFI signals. In return, our improved knowledge of radiometer data signatures will benefit us in developing effective RFI mitigation solutions through instrument modification or data analysis. To this end, we analyzed channel correlation, information content, and principal components of WindSat and SMMR data. The "RFI-free" SMMR data provided us an opportunity to contrast RFI signatures from natural radiation. Based on these analyses, we developed WindSat RFI detection algorithms using principal component analysis and a channel regression technique. Different from the spectral difference technique that use a pair of channels, the new algorithms use multichannel data analysis and are effective in detecting RFI over both land and ocean. However, the advantage of such a multivariate approach cannot be fully validated without direct comparison with RFI *in situ* data. During the joint Soil Moisture Experiment/Polarimetry Land Experiment in June–July 2005, we collected a large amount of RFI *in situ* data using an airborne radiometer and a ground-based RF emitter survey [17]. We plan to use such a dataset to validate different RFI detection techniques in our future studies.

Acknowledgment

The authors wish to thank E. Twarog (NRL) and K. St. Germain and S. Mango (IPO) for helpful discussion.

References

[1] E. Njoku, J. M. Stacey, and F. T. Barath, "The SEASAT scanning multichannel microwave radiometer (SMMR): Instrument description and performance," *IEEE J. Ocean. Eng.*, vol. 5, pp. 100–115, 1980.

[2] J. P. Hollinger, J. L. Peirce, and G. A. Poe, "SSM/I instrument evaluation," *IEEE Trans. Geosci. Remote Sens.*, vol. 28, pp. 781–790, 1990.

[3] T. Kawanishi, T. Sezai, Y. Ito, K. Imaoka, T. Takeshima, Y. Ishido, A. Shibata, M. Miura, H. Inahata, and R. Spencer, "The Advanced Microwave Scanning Radiometer for the Earth Observing System (AMSR-E), NASDA's contribution to the EOS for global energy and water cycle studies," *IEEE Trans. Geosci. Remote Sens.*, vol. 41, no. 2, pp. 184–194, Feb. 2003.

[4] P. W. Gaiser *et al.*, "The WindSat spaceborne polarimetric microwave radiometer: Sensor description and early orbit performance," *IEEE Trans. Geosci. Remote Sens.*, vol. 42, no. 11, pp. 2347–2361, Nov. 2004.

[5] D. B. Kunkee, N. S. Chauhan, and J. J. Jewell, "Phase one development of the NPOESS Conical-Scanning Microwave Imager/Sounder," in *Proc. IGARSS*, vol. 2, Toronto, ON, Canada, 2002, pp. 1005–1007.

[6] M. Genger, N. S. Chauhan, and D. B. Kunkee, "NPOESS Conical Microwave Imager Sounder: RFI issues and progress," in *Proc. IGARSS*, vol. 4, Anchorage, AK, 2004, pp. 2443–2445.

[7] L. Li, E. Njoku, E. Im, P. Chang, and K. St. Germain, "A preliminary survey of radio-frequency interference over the U.S. in Aqua AMSR-E data," *IEEE Trans. Geosci. Remote Sens.*, vol. 42, no. 2, pp. 380–390, Feb. 2004.

[8] E. Njoku, P. Ashcroft, T. Chan, and L. Li, "Global survey and statistics of radio-frequency interference in AMSR-E land observations," *IEEE Trans. Geosci. Remote Sens.*, vol. 43, no. 5, pp. 938–947, May 2005.

[9] S. W. Ellingson and J. T. Johnson, "A polarimetric survey of radio-frequency interference in C- and X-bands in the continental United States using WindSat radiometry," *IEEE Trans. Geosci. Remote Sens.*, vol. 44, no. 3, pp. 540–548, Mar. 2006.

[10] N. Grody, "Classification of snow cover and precipitation using the Special Sensor Microwave Imager," *J. Geophys. Res.*, vol. 34, pp. 7423–7435, 1991.

[11] L. Li, E. Im, and E. G. Njoku, "Radio-frequency interference (RFI) identification and suppression of the 7-GHz AMSR-E channels for land remote sensing," Jet Propulsion Lab., Pasadena, CA, D-24839, 2002.

[12] K. Knowles, E. Njoku, R. Armstrong, and M. J. Brodzik, "Nimbus-7 SMMR Pathfinder daily EASE-Grid brightness temperatures," Nat. Snow Ice Center, Boulder, CO, 2002. Digital media and CD-ROM.

[13] I. T. Jolliffe, *Principal Component Analysis*. New York: Springer-Hill, 1976.

[14] D. A. Rothrock, D. R. Thoms, and A. S. Thorndike, "Principal component analysis of satellite passive microwave data over sea ice," *J. Geophys. Res.*, vol. 93, pp. 2321–2332, 1988.

[15] M. H. Bettenhausen, C. K. Smith, R. M. Bevilacqua, N. Wang, P. W. Gaiser, and S. Cox, "A nonlinear optimization algorithm for Windsat wind vector retrievals," *IEEE Trans. Geosci. Remote Sensing*, vol. 44, no. 3, pp. 597–610, Mar. 2006.

[16] F. Wentz, private communication, 2004.

[17] Soil Moisture Experiment 2005 and Polarimetry Land Experiment (SMEX05/POLEX): Experiment Plan (2005, Jun.). [Online]. Available: http://hydrolab.arsusda.gov/smex05.

Li Li (M'96) received the M.S. degree from Beijing University of Posts and Telecommunications, Beijing, China, and the Ph.D. degree from the University of Washington, Seattle, in 1987 and 1995, respectively, both in electrical engineering.

He is currently with the Naval Research Laboratory, Washington, DC, working on spaceborne radiometry of land and oceans, particularly the algorithm development for the polarimetric microwave radiometer onboard the WindSat satellite. From 1997 to 2004, he was a Senior Scientist with the Jet Propulsion Laboratory, California Institute of Technology, Pasadena, where he participated in several NASA projects, including the Aqua Advanced Microwave Scanning Radiometer (AMSR-E), CloudSat Cloud Profiling Radar (CPR), and the JPL second-generation Precipitation Radar. From 1995 to 1997, he was with the Caelum Research Corporation, Rockville, MD, working at the Office of Research and Applications, National Environmental Satellite, Data and Information Service, National Oceanic and Atmospheric Administration (NOAA/NESDIS), Camp Springs, MD, where he conducted research in the area of polarimetric microwave radiometry, especially for the concept study of ocean surface wind vector sensing. He was a Student Visitor from 1993 to 1995 at the National Center for Atmospheric Research, Boulder, CO. His research interests include passive and active remote sensing of land and ocean surfaces for applications related to climate study and monitoring.

Dr. Li is a member of the American Geophysical Union, the IEEE Geoscience and Remote Sensing Society, and Eta Kappa Nu. He has been a recipient of the NCAR/RAP Fellowship 1993–1995 and the NASA Group Achievement Award and JPL Technical Excellence Award, both in 2002.

Peter W. Gaiser (S'91–M'93–SM'04) received the B.S. degree in electrical engineering from Virginia Polytechnic Institute and State University, Blacksburg, in 1987, and the Ph.D. degree from the University of Massachusetts, Amherst, in 1993, where he studied microwave remote sensing, with emphasis on synthetic aperture interferometric radiometry.

He has been with the Naval Research Laboratory (NRL), Washington, DC, since 1993, and currently Acting Head of the Remote Sensing Physics Branch, Remote Sensing Division at NRL. While at NRL, he has been involved in polarimetric radiometry research. His research interests also include instrument design, data collection, and model development specifically for the purpose of ocean wind vector measurements from space. He is the Principal Investigator for the WindSat spaceborne polarimetric microwave radiometer demonstration project.

Michael H. Bettenhausen (S'88–M'95) received the B.S., M.S., and Ph.D. degrees in electrical engineering from the University of Wisconsin, Madison, in 1983, 1990, and 1995, respectively. His graduate research focussed on theoretical and computational studies of radio-frequency heating in plasmas.

While employed by Mission Research Corporation, Santa Barbara, CA, from 1997 to 2000, he did software development and algorithm research for particle simulation. In 2000, he joined Integrated Management Services, Inc., Arlington, VA, where he worked on projects for analysis and processing of hyperspectral remote sensing data. He joined the Remote Sensing Division, Naval Research Laboratory, Washington, DC, in 2002. His current research interests include development of forward models and retrieval algorithms for the WindSat polarimetric microwave radiometer.

William Johnston, photograph and biography not available at the time of publication.